White Rose Research Online

eprints@whiterose.ac.uk
https://eprints.whiterose.ac.uk
Universities of Leeds, Sheffield and York

Deposited via The University of Leeds.

White Rose Research Online URL for this paper:
https://eprints.whiterose.ac.uk/id/eprint/162287/

Version: Accepted Version

Article:
Besselink, R, Stawski, TM, Freeman, HM et al. (2020) Mechanism of Saponite Crystallization from a Rapidly Formed Amorphous Intermediate. Crystal Growth & Design, 20 (5). pp. 3365-3373. ISSN: 1528-7483

https://doi.org/10.1021/acs.cgd.0c00151

© 2020 American Chemical Society. This is an author produced version of an article published in Crystal Growth & Design. Uploaded in accordance with the publisher's self-archiving policy.

Reuse
Items deposited in White Rose Research Online are protected by copyright, with all rights reserved unless indicated otherwise. They may be downloaded and/or printed for private study, or other acts as permitted by national copyright laws. The publisher or other rights holders may allow further reproduction and re-use of the full text version. This is indicated by the licence information on the White Rose Research Online record for the item.

Takedown
If you consider content in White Rose Research Online to be in breach of UK law, please notify us by emailing eprints@whiterose.ac.uk including the URL of the record and the reason for the withdrawal request.

UNIVERSITY OF LEEDS
University of Sheffield
UNIVERSITY of York

Mechanism of saponite crystallization from a rapidly formed amorphous intermediate

Rogier Besselink,*[a,b] Tomasz M. Stawski,[*,a,c] Helen M. Freeman,[a,d] Jörn Hövelmann,[a,e] Dominique J. Tobler,[f] Liane G. Benning.[a, g, h]

[a]German Research Center for Geosciences, GFZ, Telegrafenberg, 14473, Potsdam, Germany

[b]University Grenoble Alpes, University Savoie Mont Blanc, CNRS, IRD, IFSTTAR, ISTerre, 38000 Grenoble, France

[c]Bundesanstalt für Materialforschung und -prüfung (BAM), Division 1.3: Structure Analysis, Berlin, Germany

[d]School of Chemical and Process Engineering, University of Leeds, LS29JT, Leeds United Kingdom.

[e]New affiliation jorn

[f]Nano-Science Center, Department of Chemistry, University of Copenhagen, Copenhagen, Denmark

[g]Department of Earth Sciences, Free University of Berlin, 12249 Berlin, Germany

[h]School of Earth and Environment, University of Leeds, Leeds, United Kingdom

Supporting Information Placeholder

ABSTRACT: Clays are crucial mineral phases in Earth's weathering engine, but we do not know how they form in surface environments under (near-)ambient pressures and temperatures. Most synthesis routes, attempting to give insights into the plausible mechanisms, rely on hydrothermal conditions, yet many geological studies showed that clays may actually form at moderate temperatures (< 100 °C) in most terrestrial settings. Here, we combined high-energy X-ray diffraction, infrared spectroscopy and transmission electron microscopy to derive the mechanistic pathways of the low-temperature (25-95 °C) crystallization of a synthetic Mg-clay, saponite. Our results reveal that saponite crystallizes via a two stage process: 1) a rapid (several minutes) co-precipitation where ~20 % of the available magnesium becomes incorporated into an aluminosilicate network followed by 2) a much slower crystallization mechanism (several hours to days) where the remaining magnesium becomes gradually incorporated into the growing saponite sheet structure.

1. INTRODUCTION

Clay minerals are hydrous aluminum phyllosilicates rich in Fe, Mg, Ca and K, and characterized by high cation exchange and high sorption capacities. Clays predominantly form during the weathering of igneous aluminosilicate minerals (e.g., feldspars, amphiboles, pyroxenes, feldspathoids and olivine), driven by fluid-rock interactions with CO_2-acidified waters. As such clays play an important role in global cycles of various elements e.g. iron, magnesium, potassium calcium and carbon,[1-4] and are key Fe and Mg sources for vegetation. Due to their excellent properties, clays also find wide application in industry, for example in catalysis, waste storage and confinement, paper industries, oil drilling, foundry molds and pharmaceuticals.[2, 5-6]

The synthesized samples were characterized by transmission electron microscopy (equipped with energy-dispersive X-ray spectroscopy), Fourier transform infrared spectroscopy, X-ray diffraction, high-energy X-ray diffraction, and the cation exchange capacity was measured with methylene blue adsorption. The details are described in the SI: Supporting Materials and Methods.

In this work, we are focusing on smectites, the most common clays in natural soils and sediments,[5] and more specifically, on saponite, the Mg-rich trioctahedral smectite. Saponite is well-known for its low friction coefficient,[7] high surface area,[8-10] high cation exchange capacity[8-10] and catalytically active acidic surface sites.[11-13] In nature, saponite is frequently found in deep-sea hydrothermal vents, with water pressures up to 1.1 kbar. Importantly, however, together with other phyllosilicates, saponite was also found in chondritic meteorites,[14-16] dwarf planet Ceres,[17] and on Mars,[18-19] suggesting that it can also form in water-scarce and under relatively low temperature/pressure conditions (< 100 °C). However, so far, we do not fully understand how saponite forms under such geologically mild conditions.

Saponite and other smectites are typically synthesized under hydrothermal conditions,[6, 20] and in the presence of metal alkoxide precursors (e. g. aluminum, tri-isopropoxide, and tetraethylorthosilicate); conditions that are not found in nature.[6, 20] A selected number of studies successfully synthesized saponite at moderate temperatures using inorganic salts, provided that small organic molecules or 3rd ions were added to the synthesis.[21-24] For instance, Schumann et al.[25] observed saponite formation at 60 °C in the presence of oxalic acid, which led them to suggest that organic acids are a prerequisite for clay formation in carbonaceous chondrites. Baldermann et al.[24] observed that small Fe^{2+}/Si-ratios stabilized the saponite structure at temperatures as low as 60 °C. Noteworthy, however, that in both these studies the applied synthesis also induced brucite ($Mg(OH)_2$) formation at high pH, which constitutes parallel competitive processes to the clay formation.[24] Even though brucite may be formed in parallel under natural conditions, the presence of such impurities makes it more complex to study the saponite crystallization mechanism.

Vogels et al.[8] successfully avoided brucite formation by using a two-step synthesis approach: 1) formation of an aluminosilicate gel at high pH ≈ 13, and 2) maturation of the gel into saponite at pH 7 – 8 and 90 C. The reason for the absence of brucite in this synthesis is due to the use of urea at a temperature of 90 °C, allowing slow urea degradation to ammonia and hence controlled hydrolysis of Mg, which in turn enables gradual saponite formation while avoiding fast pH increase (i.e. brucite formation). To consider here further is that Al first forms a 4-fold coordination at high pH.[29] This precursor aluminosilicate gel thus simulates well the 4-fold coordinated Al in aluminosilicate (e.g., volcanic glass or olivine)[2, 4] from which saponite generally forms in nature.

The synthetic route proposed by Vogels could be a plausible analog for natural saponite formation. Nevertheless, the mechanistic and structural details of the aforementioned processes are not well understood from the point of the crystal growth chemistry. For instance, it is not clear if there are any intermediate solid phases (either amorphous or nanocrystalline) involved, and what factors limit the crystallization rate. Here, we demonstrate that the saponite's growth includes an intermediate phase, as is evidenced by the high-energy X-ray diffraction data collected from the samples quenched at several stages of the reaction. The presence of such a phase was further supported by transmission electron microscopy, which revealed the presence of amorphous spherical globules before it transformed into smectite-like sheets with well-defined interlayer distances.

2. MATERIALS AND METHODS

Saponite clays were synthesized following a slightly modified two-step synthesis procedure as described in Vogels et al,[8] which involved the formation of an amorphous aluminosilicate (SI Scheme S1: Step 1) followed by crystallization of saponite (SI Scheme S1: Step 2). For saponite synthesis, following stock solutions were prepared using reagent grade chemicals and deionized water (DIW, 18 MΩcm): $Na_2SiO_3 \cdot 5\ H_2O$ ([Si] = 1.2 M, Sigma-Aldrich >95%), $AlCl_3 \cdot 6\ H_2O$ ([Al] = 1 M, VWR, ACS), $MgCl_2 \cdot 6\ H_2O$ ([Mg] = 1.2 M, VWR, ACS), urea (5 M, Carl-Roth GmbH & Co, 99.5%), NaOH (5 M, VWR, ACS) and hydrochloric acid (2 M, Carl-Roth, 37% p.a.). A 0.4 M histidine·HCl stock solution was prepared by dissolving L-histidine (VWR, 99%) and hydrochloric acid in an equimolar ratio in DIW. Here, histidine was used as a buffer to avoid a fast pH decrease upon adding hydrochloric acid. As is explained in the introduction, urea was added to enable hydrolysis of magnesium by a slow release of ammonia, while avoiding a fast pH increase. Then, saponite was synthesized by a two-step procedure as described below and visually illustrated with a flow diagram (SI, Scheme S2).

Step 1: An aluminosilicate gel with [Si]:[Al]:[OH] = 6.8/1.2/6.0 was prepared by mixing 2.10 mL of 1 M $AlCl_3$ and 2.10 mL 5 M NaOH solution (mixed, stirred until the solution was clear), which was then added drop-wise to 9.92 mL 1.2 M Na_2SiO_3 solution under vigorous stirring, at room temperature. The mixture was heated for 1 h at 100 °C under a reflux condenser to avoid water loss.

Step 2: The aluminosilicate gel was cooled down to 25 °C in a water bath and diluted with 35.9 mL water to yield a total volume of 50 mL. In a separate bottle 8.40 mL 5 M urea, 8.75 mL 1.2 M $MgCl_2$, 8.75 mL 0.4 M histidine hydrochloride and 9 mL 2 M hydrochloric acid were all mixed and diluted with DIW to 50 mL. The mixture was poured into the diluted aluminosilicate suspension under vigorous stirring. The mixture was then neutralized to a pH between 6.8 and 7.2, with roughly 1.5 mL 2 M hydrochloric acid and subsequently heated to 95 °C using a preheated oil bath (T = 100 °C) and a reflux cooler system. Due to the fact that the suspension was not very stable at pH 7 and 25 °C, it was important to execute the mixing and pH neutralization within ~10 min (i.e. the gel had to be fresh since Al^{3+} will slowly dissolve and becomes 6-fold coordinated). Once the target temperature was reached (~ 15 min), the time was set to 0 and the crystallization reaction held at this temperature for various time durations (5 min to 90 d). Afterward, the suspensions were cooled to room temperature and then centrifuged (10 min at rcf ≈ 9.5 kG) to isolate the solids. The supernatant was discarded and the solids re-suspended in DIW. This washing procedure was repeated 3 times to remove any residual salts. The majority of the solid paste was placed into a desiccator to dry for 5 d (10-30 mbar, 25 °C). For glycolization, selected dried solids and glycol were placed inside a desiccator kept at 60 °C and ~ 10 mbar. By using the same approach, samples were also synthesized at 60 °C and 25 °C. In a separate set of experiments the Mg concentration was increased to yield a [Mg]:[Si] = 12:6.8, while keeping the total volume constant.

3. RESULTS AND DISCUSSION

Saponite was synthesized in two separate reaction steps, i.e. (Step 1) the formation of an amorphous aluminosilicate network, (Step 2) the crystallization of the amorphous network towards saponite in the presence of magnesium and urea. Our preliminary observations of the reaction in Step 2 suggested that the amorphous aluminosilicate gel reacted very fast at its surface with magnesium, but it did not immediately crystallize to saponite. This reaction step was subdivided into two substages.

3.1. Synthesis step 1: The formation of an amorphous aluminosilicate gel

The gel that formed immediately after mixing the silicate and aluminate solutions, was composed of spheroidal aggregates/particles or globules ranging in diameter from 50 to 200 nm as revealed by TEM imaging (Fig. 1a). These aggregates did not contain any sharp edges or lattice fringes, indicating that the material was amorphous. This was also confirmed by XRD which showed a broad maximum at d = 3.09 Å (Cu-Kα 2θ = 28.9°, α in Fig. 2, pattern I) stemming from the Si-Si and Si-Al distances common in amorphous aluminosilicates with dihedral Si-O-Si angles of 150° and the Si-O and Al-O distances close to 1.60 Å.[27-28] The auxiliary FTIR spectrum contains both in-phase and out-of-phase antisymmetric Si-O vibrational modes (SI: Fig. S1, Tabel S1), which is consistent with an amorphous aluminosilicate as discussed in more detail in the SI. Moreover, in TEM imaging these structures typically exhibited heterogeneities, with the cores being more electron transparent (brighter) compared to the rims. EDS analysis indicated that the brighter regions were depleted in Na compared to the darker rims (SI: Table S2). Furthermore, the aggregates overall were depleted in Al with respect to the initial Al: Si ratio (1.2:6.8), indicating that the available Al was not stoichiometrically incorporated into the precursor aluminosilicate gel.

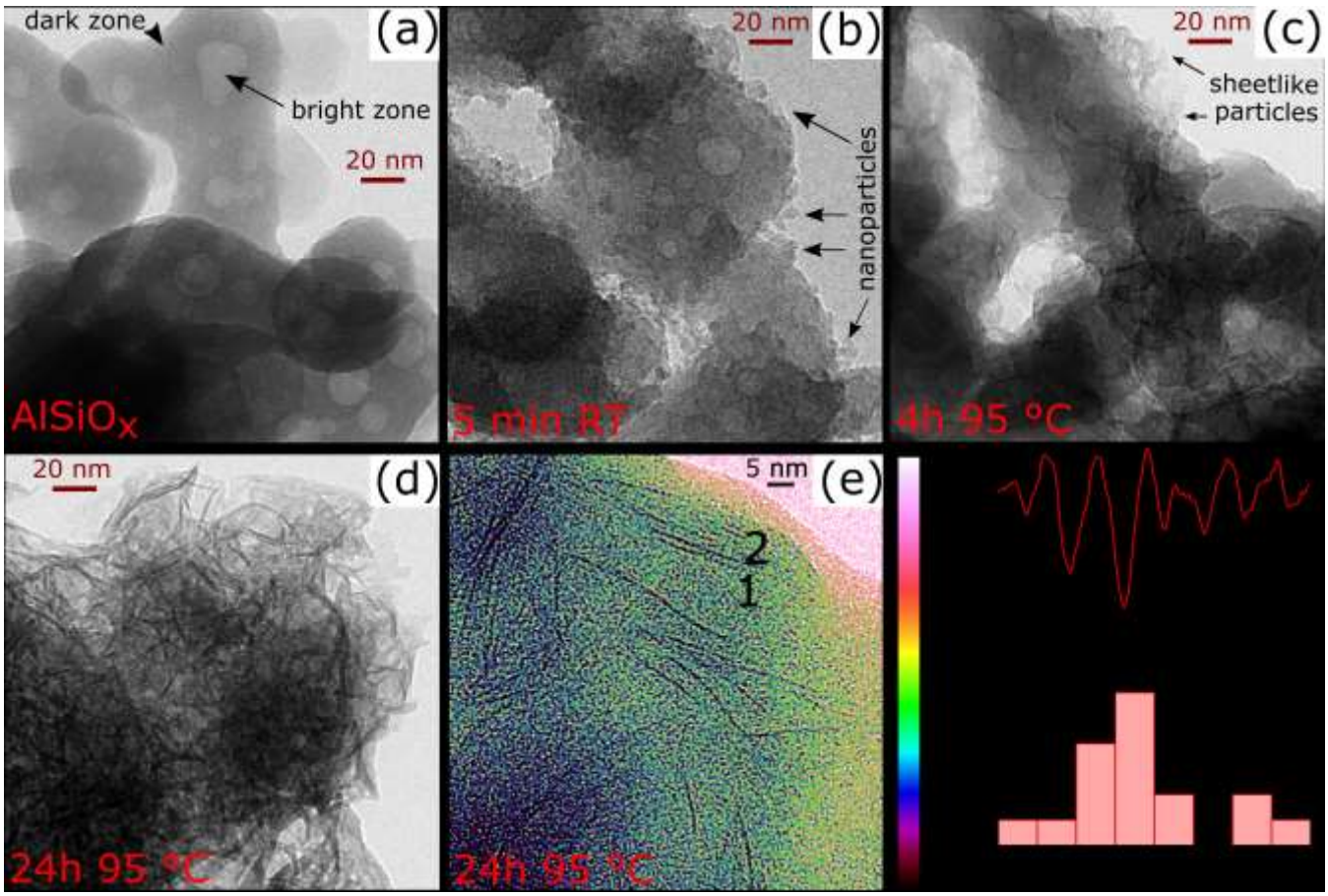

Figure 1. (a)-(d) Bright-field TEM images of solids removed at different sub-stages during saponite crystallization: (a) precursor aluminosilicate gel; (b) 5 min after mixing $MgCl_2$ and aluminosilicate gel at 25 °C; (c) after 4 h crystallization at 95 °C; (d) after 24 h crystallization at 95 °C. (e) TEM image (with false-color intensity scaling) of 24 h/95 °C saponite dispersed in cured LR-white, with saponite stacks; (f) distance profile from sheets indicated by numbers 1, 2 in (e); (g) histogram of distances between sheets from 17 different particle stacks, which indicates an averaged interlayer distance of 1.3 nm

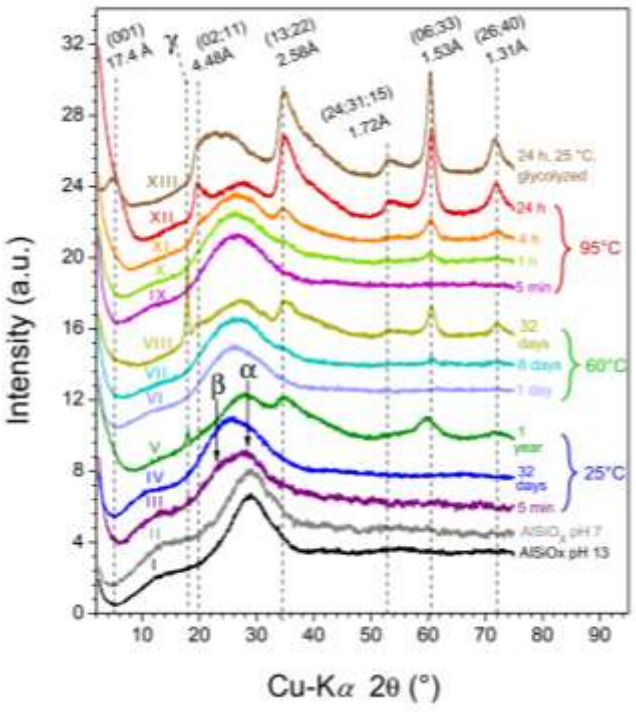

Figure 2. XRD patterns of synthesis products from the various substages of the crystallization step at 5, 60, and 95 °C; the reflections with α and β refer to correlation peaks originating from metal-metal distances, i.e., α relates to tetrahedral metal cation distances (^{IV}Si, ^{IV}Al) and β relates to octahedral metal cation distances (^{VI}Mg, ^{VI}Al); the peak marked with γ corresponds to a gibbsite impurity in the long-term synthesis products at 25 °C and 60 °C.

3.2. Synthesis step 2, sub-stage 1: Reaction of magnesium at the surface of the aluminosilicate.

Immediately after pH neutralization and $MgCl_2$ addition but prior to heating, small nanosized particles were formed at the surface of the aluminosilicate particles as revealed by TEM imaging (< 20 nm, Fig. 1b). In addition, a new broad reflection was observed in the XRD pattern at d = 3.77 Å, (Cu-Kα 2θ = 23.6°, β in Fig. 2, pattern III). This reflection corresponds to distances larger than Si-O-Si/Al bonds and is best explained by the formation of Mg-O bonds, ~2.05 Å.[33] This is also supported by the fact that this reflection was absent in a sample of the aluminosilicate gel which was neutralized but not mixed with the $MgCl_2$ solution (Fig. 2, pattern II).

3.3. Synthesis step 2, sub-stage 2: Crystallization of saponite.

After 4 h of reaction at 95 °C, the nanoparticle – gel mixture still contained mostly spherical aluminosilicate aggregates but in addition sheet-like particles also appeared (Fig. 1c). After another 20 h (Fig. 1d), the original morphology fully disappeared and only the sheet-like particle morphology persisted. Thus, during this period, amorphous aluminosilicate gradually transformed into a layered structure as evidenced by the 24 h/95 °C sample. We embedded this product in an acrylic resin, which allowed us to visualize and measure distances between individual sheets (Figs. 1 e, f). The average sheet-to-sheet distance (as determined from 17 different stacks) was 1.37 ± 0.37 nm (Fig. 1g), which is consistent with typical interlayer distances for smectite clays.[24, 29]

The transformation of the material towards a smectite-type clay was also evidenced by the appearance and progressive growth of smectite-like reflections in XRD patterns (Fig. 2, patterns IX-XIII).[24, 30-31] The asymmetric nature of the peaks with *hk*-indices (13;22) and (24;31;15) are indicative of substantial turbostratic disorder, which involves both translational and rotational disorder in the stacking of the sheets on top of each other.[32] Meanwhile, the FTIR spectrum (SI: Fig. S1, Table S1) reveals the presence of the (Mg)OH liberation mode that is associated with a trioctahedral clay structure and narrowing of the antisymetric SiO vibration that is associated with a reduced disorder of the silica network (as discussed in more detail in the SI). The (001) reflection was only observed for the glycolized sample (Fig. 2, XIII), at d = 17.4 Å (Cu Kα 2θ = 5.3°), and matched the interlayer spacing of smectite-like clays with an interlayer charge z < 1.2 per $[Mg;Al]_6$ $[Si;Al]_8O_{20}(OH)_4$ unit.[31-32] The position of the (06;33) reflection, corresponding to a spacing of d = 1.53 Å, is consistent with the interlayer spacing of a trioctahedral clay structure.[31-32]

At lower synthesis temperatures (25 and 60 °C) similar smectite type features were formed, however, the reaction kinetics were much slower. This is shown by comparison of the XRD patterns in Fig. 2: the 4-hour pattern at 95 °C matched the 32-day pattern at 60 °C and the 1-year pattern at 25 °C in terms of peak location and intensity (all measured at the same conditions, and for the same amounts of solid). The only visible difference was a diffraction peak at 2θ = 17.9°, stemming from gibbsite (4.82 Å, (002)), that emerged in samples after a long reaction time (γ in Fig. 2, V and VIII). Note that no other secondary phases (e.g. talc and chlorite interstratifications) were observed. Thus, we can confirm that saponite can form at ambient temperatures (< 95 °C).

3.4. Detailed evolution of the local atomic structure upon saponite crystallization.

More detailed information regarding the local environment of atoms was obtained from the HEXD measurements and their PDF analysis (SI: Fig. S2). The PDF of the final product after 19 d at 95 °C (Fig. 3a, black pattern labeled with (I)) can be compared with simulated saponite profiles (Fig. 3a II-IV) from its structure (Fig. 3b).[41] In these PDF profiles, the distance at 1.63 Å is associated with T-O distances, where T represents Al and Si cations tetrahedrally coordinated by oxygen.[33] This characteristic distance is typical for silicates and unsurprisingly was found in all our samples.

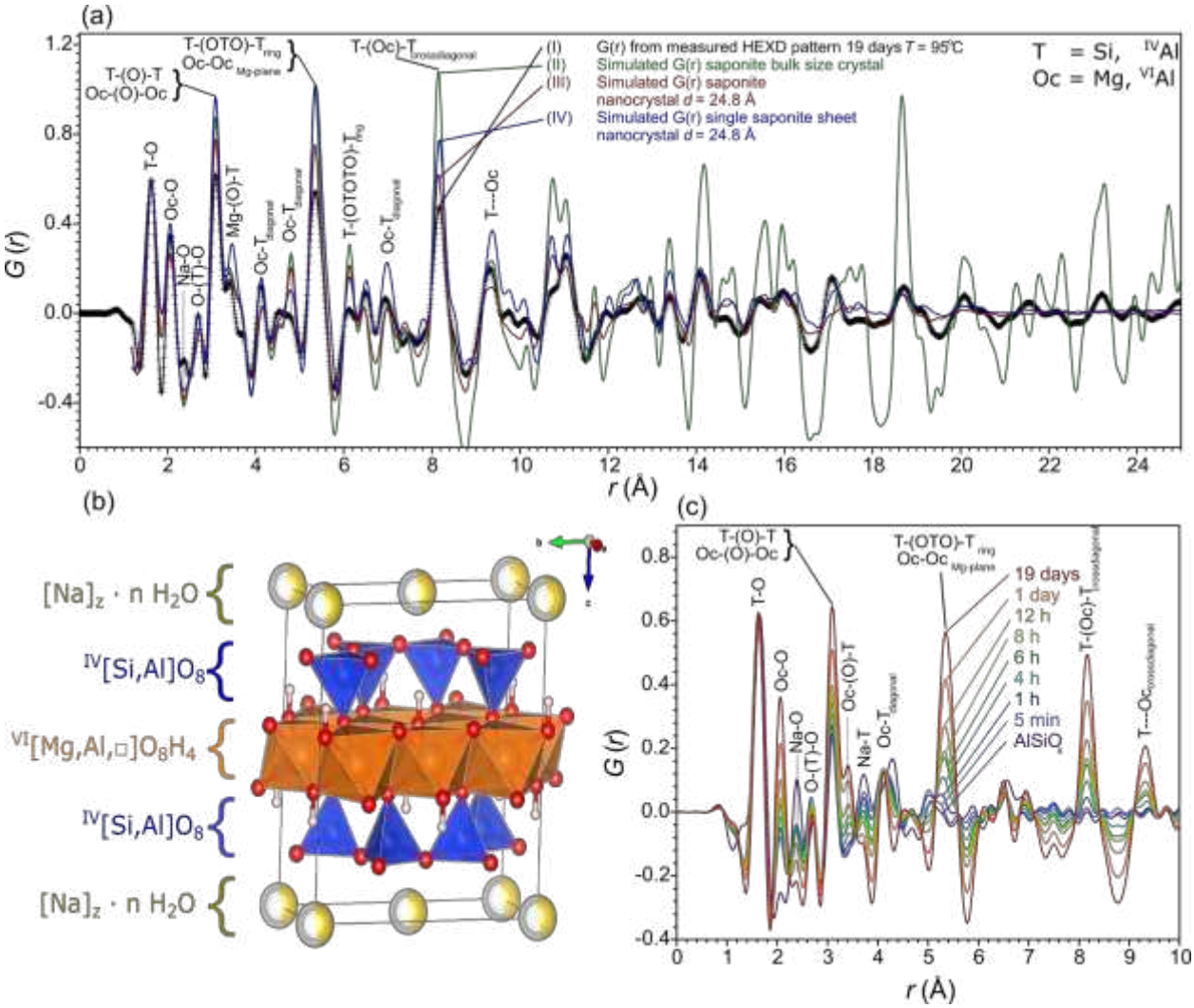

Figure 3. (a) PDFs of I) samples reacted for 19 d at 95 °C (see more info also in SI, Fig. S2); II) simulated G(r) of a saponite structure,[33] with a modified stoichiometry (from SI: Table S3), and with cell parameters and anisotropic displacement parameters optimized to the experimental data, while keeping relative atom positions constant; III) simulated G(r), nanocrystal size damping ~25 Å of curve (II); IV) simulated PDF pattern of a saponite sheet by placing the saponite sheet from II in a unit cell with an extended c-axis and consequently eliminating cross-correlations from neighboring sheets and sodium ions. For the sake of comparison, all simulated (II-IV) and measured PDF patterns (I) were normalized against the T-O peak intensity of a 19-d-saponite (I); (b) Simulated generalized type-II trioctahedral saponite structure[41]; (c) PDFs from measured total scattering curves of samples reacted at 95 °C for between 5 min to 19 d, including the PDF pattern of the precursor aluminosilicate gel. All simulated and measured PDF patterns were normalized against the T-O peak intensity of the 19 d/95 °C saponite.

The decrease in correlation intensity with increasing distances was more evident for the experimental data compared to the simulated PDF of bulk saponite crystal. To a large extent, this can be explained by the fact that the synthesized saponite consisted of nanocrystals and this effect is largely reproduced in the simulated profiles by introducing a limited particle size diameter of ~25 Å that suppressed higher distance correlations (Fig. 3a III). On the other hand, many distance correlations of the experimental PDF were also present in the simulated curves (Fig. 3a II-IV) except for the correlations at 2.38 and 3.66 Å. The distance at 2.38 Å matched with Na-O distances pairs in crystalline tectosilicates (e.g., hydrosodalite, pitiglianoite and cancrinite[33]) and its intensity substantially decreased during the transformation into more crystalline silicates (Fig. 4c). Based on TEM-EDS analyses (SI: Table S2) roughly half of the fraction of sodium ions leached out within the first 5 min of reaction, which likely explains the first decrease in Na-O pair intensity.

For the longer reaction times, the tectosilicate-type Na-O pair intensity (at 2.38 Å) further decreased, whereas TEM-EDS indicated that the Na fraction remained constant after 24 h (SI: Tables S2 and S3). Consequently, the second decrease of the Na-O pair intensity can be associated with the rearrangement of sodium ions into different lattice positions. Moreover, Na-O pair distances are probably larger for phyllosilicates as it was observed for instance for nontronite with Na-O pairs at distances in a range between 2.8 and 3.4 Å.[33] Thus, two effects coincide: at short reaction times, sodium predominantly leaches out of the aluminosilicate gel, whereas after longer reaction periods sodium ions rearrange into interlayer position.

The peak at 3.66 Å most likely relates to Na-T pairs despite being larger than the expected distance in tectosilicates (d(Na-T) = 3.40 Å).[33] However, the Na-O-T bond angles (∠(Na-O-T) ≈ 131°) in disordered framework silicates are larger compared to well crystalline tectosilicates (∠(Na-O-T) ≈ 115°), which in turn could explain the larger Na-T distance. The pair distance correlation at 2.68 Å corresponds to O-(T)-O distances for both tecto- as well as phyllosilicates, and these intensities remain roughly constant throughout the crystallization reaction. Finally, pair distance correlations at 2.06 and 3.38 Å are associated with Oc-O bonds and Oc-(O)-T distances of the modified saponite structure, where Oc represented octahedral metal cations, Mg and ^{VI}Al. The intensity of these distance correlations increases with increasing reaction time, which is likely a consequence of condensation of magnesium and octahedral aluminum into the aluminosilicate framework. Based on the simulated structures, next-nearest neighbors were assigned to correlations at given distances (Fig. 4a), which could be subdivided into in-plane correlations at 3.04, 5.34 and 6.11 Å, and cross-diagonal plane correlations at 3.47, 4.09, 4.78, 6.10, 6.99, 8.18 and 9.36 Å.

The slight disagreement between the experimental and the simulated PDF of saponite nanocrystals (Fig. 3a III) indicates structural imperfections in the synthesized saponite (Fig. 3b). This might be due to turbostratic disorder (i.e., faults in the stacking of the sheets). To explore this we calculated the PDF of an isolated saponite sheet with a c-axis extended to 100 Å, while keeping absolute atom positions fixed (Fig. 3a IV). The juxtaposition with our data showed that most of the observed distance correlations in the measured data match the ones from the simulated single sheet, indicating that our data do not actually exhibit correlations across sheets, thus it is unaffected by the stacking of the sheets. Consequently, the reduced correlations in our data (Fig. 3a I) when compared to the simulated sheet pattern (Fig. 3a IV) cannot fully be explained by turbostratic defects or reduced crystal domain sizes. Thus, this discrepancy between data and model may also be due to defects within the sheet structure, such as a ditrigonal distortion, cation substitution and/or cation vacancies as are also seen in other clay systems.[31, 34-36]

The presence of defects due to cationic substitution can be evaluated through the compositional analysis from TEM-EDS and by solving charge and mass balances equations (see SI: Supporting Data Analyses). Consequently, the fractions of 4-fold-coordinated $^{IV}Al^{3+}$ and 6-fold-coordinated $^{VI}Al^{3+}$ were estimated. The EDS measurements were carried out on two saponite samples synthesized at 95 °C for 24 h and 19 d. Both the 24 h and the 19d samples had a reduced rMg ratio and an enlarged rSi ratio compared to the idealized composition: $Na_{1.2}[Si_{6.8}{}^{IV}Al_{1.2}][Mg_6]O_{20}(OH)_4$ (SI: Table S3). Moreover, the Na content and the cation exchange capacity (CEC) were lower compared to the ideal composition, which suggested a reduced interlayer charge. This can be expected when aluminum partially occupies the octahedral position (^{VI}Al) and forms a type-II saponite as illustrated in SI: Scheme S2b. The 19 d sample has an increased ^{IV}Al concentration in comparison to the 24h sample, which suggests slow incorporation of additional Al^{3+} ions on tetrahedral sites. As a consequence, the CEC of saponite and the Na^+ fraction in the interlayer increased going from 24 h to 19 d (SI: Table S3).

3.5. Reaction Kinetics and proposed mechanism of saponite formation.

The time-dependent change in XRD peak intensities was used to estimate the rate of saponite crystallization for each tested synthesis temperature (25, 60 and 95 °C, Fig. 4a). The reaction progress was best described by the first-order reaction rates (Fig. 4a and SI: Table S4). Since the reaction kinetics were similar for two different magnesium concentrations (Fig. 5a. 95 °C, Mg_6 and Mg_{12}), we can clearly state that the condensation of magnesium into the aluminosilicate network is not the rate-limiting process (see also SI: Supporting Data Analyses).

Time-dependent change in the PDF normalized peaks intensities for Na-O (2.38 Å), Oc-O (2.06 Å) and T-(Oc)-T (8.18 Å) pairs (Fig. 5b) revealed that the intensity of the short-range correlations (Na-O and Mg-O) changed rapidly within the first 5 min. In contrast, the T-(Oc)-T pair at 8.18 Å only reveals a significant change after ~ 1 h of reaction similar to the other longer-range correlations (Fig. 3b). These trends indicate that the ordering and crystallization reactions proceed via a two-stage-process. The first stage involves a fast re-structuring of short-range distances, where Na^+ ions rearrange and $[Mg^{2+}\cdot n\ H_2O]$ condense into a disordered aluminosilicate network, which is completed within the first 5 min at 95 °C. During this stage, 70% of the Na-O bonds became rearranged (Fig. 4b) and TEM-EDS analysis (SI: Table S3) indicated that ~ 50% of the Na ions remained present in the solid material. Thus, 50% of the original Na ions dissolved, 20% rearranged to different lattice positions and 30% remained at their original tectosilicate-like distances from oxygen.

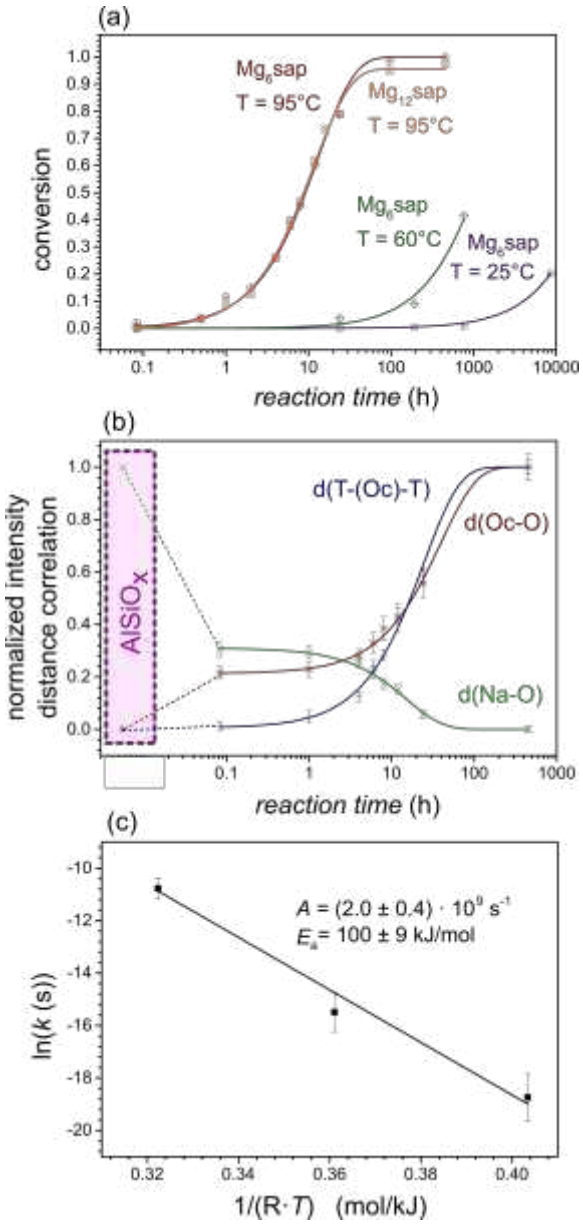

Figure 4. (a) Saponite formation rates based on overall peak intensities of powder XRD at 25, 60 and for 95 °C at two magnesium ratios, 6 and 12 per $O_{20}(OH)_4$, referred to as Mg_6sap (stoichiometric) and Mg_{12}sap (double the stoichiometric amount); (b) α and reaction progress based on distance correlations at 2.04, 2.38 and 8.18 Å corresponding to Mg-O, Na-O and T-(Mg)-T distances respectively; (c) Arrhenius plot based on reaction rates from the evaluated XRD intensities in (a)

The second stage is much slower and affects both short- and long-range atomic distances, which eventually leads to the formation of a layered sheet-like structure, with the same symmetry constraints as hectorite. During the whole process, ~20% of the Oc-O pairs was formed during the first stage and the remaining ~80% during the second stage (Fig. 4b). Meanwhile, only ~15% of the Mg^{2+} fraction within the 19 d sample was condensed to the aluminosilicate network within the first 5 min. The ~5%-difference between the Oc-O pairs and the condensed Mg^{2+} fraction is likely explained by octahedral ^{VI}Al ions that contribute to the measured pair distance at 2.06 Å. Furthermore, the Mg-O condensation and rearrangement of Na^+ ions were likely limited by the slow rate of the sheet formation as indicated by the delayed increase of the T-(Oc)-T correlation. After 24 h at 95 °C, our TEM-EDS data revealed an increased $^{IV}Al^{3+}$ and Na^+ ion concentration in the synthesized saponite (SI: Table S3) Thus, as the fraction of the incorporated $^{IV}Al^{3+}$ increases, the interlayer charge increases, allowing more Na^+ ions to diffuse into the interlayer of saponite, which stabilizes its structure.

From the data in Fig. 4a we also estimated an activation energy of crystallization te be ~100 kJ/mol (Fig. 4c). Similar activation energies were found for the transformation and hydrolysis reactions in varying types of layered silicates, including: beidelite to illite/smectite transformation,[37] Na-montmorillonite hydrolysis,[38] kaolinite to illite,[39] and the kaolinite to mullite transformations.[40] The activation energy in a range between 80 - 120 kJ/mol was associated with the disruption of Si-O bonds.[41] Our results suggest that the fraction of $^{IV}Al^{3+}$ increases during the progressive saponite crystallization. Since Al-substitution involves disruption of silicate bonds, this Si-O-bond disruption may be one of the key rate-limiting processes of saponite formation. On the other hand, diagenetic smectite to illite transformation reactions are often described as requiring lower activation energies (in the range of 37-70 kJ/mol)[42] and as such those transformations are limited by ion exchange processes and not a disruption of Si-O bonds.

3.6 Proposed mechanism of saponite formation

Based on all the data discussed above, we can summarize the process of saponite crystallization (Fig. 5). Here, a precursor aluminosilicate gel is formed in Step 1 and is composed of mixed silica/alumina tetrahedra (Figure 5a: ▾, ▾) and interconnected sodium ions (★), which are predominantly located at the outer (rim) regions of the gel. The gel is mixed with magnesium ion, which starts Step 2 of a multi-stage reaction:

Step 2, sub-stage 1: <5 minutes ~15 % of the magnesium ions condense (Fig. 6b, ♦) within the aluminosilicate framework. From the available Al ions, 50% dissolve (•), 27% rearrange into an octahedral coordination (♦) and 23% remain in the tetrahedral coordination (▾); ~ 50 % of the strongly interconnected sodium ions (Fig. 6a, b: ★) leach into solution (•) and ~20% rearrange to different lattice positions (☀).

Step 2, sub-stage 2: at a slower rate, the atoms within the amorphous aluminosilicate slowly rearrange towards a brucite-like layered trioctahedral sheet structure and the remaining magnesium ions become incorporated within the structural framework. A bit counter-intuitively, this incorporation of magnesium is not the rate-limiting step. The crystallization is in fact limited by either 1) disruption of the Si-O bonds which enables the incorporation of additional $^{IV}Al^{3+}$ ions (▾) and/or by 2) diffusion-limited separation of the octahedrally coordinated Mg and Al cations (♦,♦) from the tetrahedrally coordinated Si and Al cations (▾ , ▾ , Fig. 5b-d). Even after 19 d at 95 °C, the saponite sheets still contained many defects (as we learned from the calculated next-neighbor correlations from PDF data). Based on this proposed mechanism and the derived activation energy and reaction rates, we estimate that at 25 °C saponite would require at least 14 years to convert 95% of a precursor amorphous aluminosilicate to a trioctahedral saponite clay.

4. CONCLUSION

Our results clearly document how saponite forms from a precursor aluminosilicate gel via an amorphous intermediate Mg-rich phase where 15% of the magnesium fraction reacts within 5 min at 95 °C. This is followed by a slower crystallization to saponite, which takes more than 8 h at 95 °C. The magnesium concentration essentially does not affect the rate of crystallization but the structural arrangement to sheets seems to be the rate-limiting step in the crystallization reaction as evidenced by the delayed increase in sheet-related distance correlations compared to the Mg-O and ^{VI}Al-O distances. Hence, the process proceeds via a very fast formation of an Mg-rich amorphous intermediate that subsequently slowly reorganizes into a sheet-like structure of saponite.

ASSOCIATED CONTENT

Supporting Information

- Supporting Synthesis and Reaction Schemes (Scheme S1; Scheme S2; Scheme S3)
- Supporting Materials and Methods (Transmission electron microscopy (TEM); X-ray diffraction (XRD); Fourier-Transform Infrared Spectroscopy (FTIR); Cation exchange capacity (CEC))
- Supporting Figures (Fig. S1; Fig. S2)
- Supporting Tables (Table S1; Table S2; Table S3)
- Supporting Data Analyses (1. Assignment of FTIR vibration modes during various stages of the saponite formation, 2. Calculation of the cation substitution schemes and mass-balances to determine lattice ion occupations by TEM-EDS; 3. Kinetic models of saponite formation)

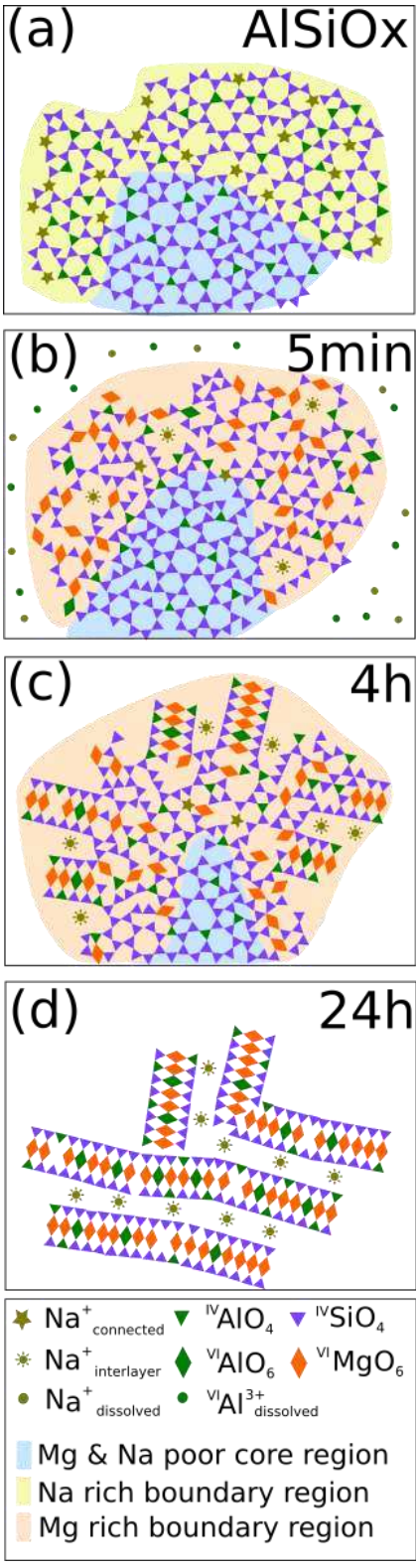

Figure 5. Schematics of the saponite crystallization: (a) AlSiOx precursor gel; (b) amorphous Mg-rich aluminosilicate gel, c) after 4 h at 95 °C with initial layered materials growing at the boundary; (d) after 24 h with the majority of material transformed to saponite.

AUTHOR INFORMATION

Corresponding Authors

* Email: besserogier@gmail.com, tomasz.stawski@gmail.com

ORCHID:
R. Besselink: 0000-0002-2027-9403-412
D. J. Tobler: 0000-0001-8532-1855
T.M. Stawski: 0000-0002-0881-5808
L.G. Benning 0000-0001-9972-5578

Notes

The authors declare no competing financial interest.

ACKNOWLEDGMENT

This research was funded by a Helmholtz Recruiting Initiative grant which supported R.B., T.M.S., H.M.F., J. H. and L.G.B. This research was also supported by a Marie Curie grant from the European Commission in the framework of the NanoSiAl Individual Fellowship, Project No. 703015 to T.M.S.
We also want to thank Karina Chapman, Peter Chupas, Rick Spence and Kevin A. Beyer for assistance with HEXD analyses at the APS beamline 11 ID-B. Use of the Advanced Photon Source was supported by the U. S. Department of Energy, Office of Science, Office of Basic Energy Sciences, under Contract No. DE-AC02-06CH11357. We would like to thank our GFZ colleagues for technical assistance with the XRD (Anja M. Schleicher, TEM sample preparation (Richard Wirth and Anja Schreiber) and FTIR (Ilias Efthimiopoulos and Monika Koch-Müller).

REFERENCES

1. Sun, X; Higgins, J.; Turchin, V. *Mar. Geol.*, **2016**, *373*, 64-77
2. Zhou, C. H.; Keeling, *J. Appl. Clay Sci*. 2013, *74*, 3-9
3. Merriman, D. *Geol. Today*, **2002**, *18* (2), 67-71
4. Hazen, R. M.; Sverjensky, D. A.; Azzolini, D.; Bish, D. L.; Elmore, S. C.; Hinnov, L.; Milliken, R. E. *Am. Mineral*. **2013**, 98 (11-12), 2007-2029.
5. Lantenois, S.; Muller, F.; Bény, J. M.; Mahiaoui, J.; Champallier, R. *Clays Clay Miner*. **2008**, *56* (1), 39-48
6. Zhang, D.; Zhou, C.; Lin, C.; Tong, D.; Yu, W.; *Appl. Clay Sci.* **2010**, *50*, 1-11
7. Lockner, D. A.; Morrow, C.; Moore, D.; Hickman, S. *Nature* **2011**, 472, 82-85
8. Vogels, R.; Kloprogge, J. T.; Geus, J. W. *Am. Mineral.* **2005**, *90* (5–6), 931–944.
9. Wang, Y.; Su, X.; Lin, X. ; Zhang, P.; Wen, K.; Zhu, J.; He, H. *Appl. Clay Sci.* **2015**, *116-117*, 102-110
10. Kloprogge, J. T.; Breukelaar, J.; Jansen, J. B. H.; Geus, J. W. *Clays Clay Miner*. **1993**, *41* (1), 103-110.
11. Vogels, R. J. M. J.; Kloprogge, J. T.; Geus, J. W. *J. Catal.* **2005**, *231*, 443-452
12. Varma, R. S. *Tetrahedron* **2002**, *58* (598), 1235-1255
13. Casagrande, M.; Storaro, L.; Lenarda, M.; Rossini, S.; Catal. Commun. **2005**, *6*, 568-572
14. Zolensky, M.; Barrett, R.; Browning, L. *Geochim. Cosmochim Act.* **1993**, *57*, 3123-3148.
15. Brearley, A. J.; *Cheochim. Cosmochim. Acta* 1995, *59* (11), 2219-2317
16. Keller, L. P.; Thomas, K. L.; Clayton, R. N.; Mayeda, T. M., DeHart, J. M. McKay, D. S. *Geochim. Cosmochim. Acta* **1994**, *58* (24), 5589-5598,
17. Milliken, R.E.; Rivkin, A. S.; *Nat. Geosci*. **2009**, *2*, 258-261
18. Burns, R. G.; *Geochim. Cosmochim. Act*a **1993**, *57*, 4555-4574
19. Bischop, J. L.; Loizeau, D.; McKeown, N. K.; Saper, L.; Dyar, M. D.; Des Marais, D. J.; Parente, M.; Murchie, S. C. *Planet. Space Sci*., **2013**, *86*, 130–149
20. Kloprogge, J. T. *J. Porous Mater.* **1998**, *5*, 5-41
21. Decarreau, A.; Petit, S.; Martin, F.; Farges, F.; Vieillard, P.; Joussein, E. *Clays Clay Miner*. **2008**, *56* (3), 322-337
22. Harder, H. *Chem. Geology* **1976**, *18*, 169-180
23. Farmer, V. C.; McHardy, W. J.; Elsass, F.; Robert, M.; *Clays, Clay Miner.* **1994**, *42* (2), 180-186
24. Baldermann, A.; Dohrmann, R.; Kaufhold, S.; Nickel, C. Clay Miner. **2014**, *49*, 391–415
25. Schumann, D.; Hartman, H. Erbl, D. D.; Sears, S. K. Hesse, R.; Vali, H.; Astrobiology **2012**, *12* (6), 549-561
26. Tobler, D. J.; Stawski, T. M.; Benning, L. G. "Silica and alumina nanophases: natural processes and industrial applications." New Perspectives on Mineral Nucleation and Growth. Springer, Cham, 2017. 293-316.
27. Okuno, M.; Zotov, N.; Schücker, M.; Schneider, H., *J. Non-Cryst. Solids***. 2005**, *351*, 1032-1038
28. Mozzi, R. L., Warren, B. E. J. Appl. Cryst. 1969, 2, 164-172
29. Taylor, W. R. *Proc. Indian Acad. Sci.* **1990**, *99* (1), 99–117
30. Grauby, O.; Petit, S.; Decarreau, A.; Baronnet, A. *Eur. J. Miner*. **1994**, *6* (1975), 99–112
31. Steudel, A.; Friedrich, F.; Schuhmann, R.; Ruf, F.; Sohling, U.; Emmerich, K. *Minerals* **2017**, *7* (5), 1-14
32. Moore, D. M.; Reynolds, R. C. X-ray diffraction and identification and analysis of Clay minerals, Oxford University Press, Inc. New York, 1989.
33. Gražulis, S.; Daškevič, A.; Merkys, A.; Chateigner, D.; Lutterotti, L.; Quirós, M.; Serebryanaya, N. R.; Moeck, P.; Downs, R. T.; Le Bail, A. *Nucleic Acids Res*. **2012**, *40* (D1), 420–427. COD Reference numbers: hectorite: COD 9009802, hydrosodalite: 1529906, pitiglianoite: 1541228, cancrinite: 1541810, pyrophylite: 9000207, talc: 1011152, nontronite: 9006564
34. He, H. Li, T. Chen, T. Zhang, D. Jianxi, Z. Peng, Y. Zhu, R., *Am Mineral.* **2014**, *99*, 109-116
35. Kloprogge, J. T.; Breukelaar, J.; Geus, J. W.; Jansen, J. B. H. *Clays Clay Miner.* **1994**, *42* (1), 18-22
36. Cuadros, J.; Dekov, V. M. ; Fiore, S. *Am. Mineral.* **2008**, *93*, 1338-1348
37. Gualtieri, A.; Bellotto, M.; Artioli, G.; Clark, S. M. *Phys. Chem. Miner.* **1995**, *22*, 215-222
38. Shainberg, I.; *Soil. Sci. Am. Proc*, **1973**, *37*, 689-694
39. Huang, W. L. *Clays Clay Miner*.; **1993**, *41* (6), 645-654
40. Gualtieri, A.; Bellotto, M. Artioli, G.; Clak, S. M. *Phys. Chem. Miner.* **1995**, *22* 215-222
41. Lasaga, A. C.; Gibbs, G. V.; *Am. J. Sci*. **1990**, *290*, 263-295
42. Velde, B.; Vasseur, G.; *Am Mineral.*, **1992**, *77*, 967-9